Epithelial cell chirality emerges through the dynamic concentric pattern of actomyosin cytoskeleton

Takaki Yamamoto,[1,2,*] Tomoki Ishibashi,[1,*] Yuko Mimori-Kiyosue,[3] Sylvain Hiver,[4] Naoko Tokushige,[3] Mitsusuke Tarama,[1,5] Masatoshi Takeichi,[4] and Tatsuo Shibata[1,†]

[1] *Laboratory for Physical Biology, RIKEN Center for Biosystems Dynamics Research, Kobe 650-0047, Japan*
[2] *Nonequilibrium Physics of Living Matter RIKEN Hakubi Research Team, RIKEN Center for Biosystems Dynamics Research*
[3] *Laboratory for Molecular and Cellular Dynamics, RIKEN Center for Biosystems Dynamics Research, Kobe, Japan*
[4] *Laboratory for Cell Adhesion and Tissue Patterning, RIKEN Center for Biosystems Dynamics Research, Kobe, Japan*
[5] *Department of Physics, Kyushu University, Fukuoka 819-0395, Japan*

The chirality of tissues and organs is essential for their function and development. Tissue-level chirality derives from the chirality of individual cells that comprise the tissue, and cellular chirality is considered to emerge through the organization of chiral molecules within the cell. However, the principle of how molecular chirality leads to cellular chirality is still unclear. To address this question, we experimentally studied the chiral behaviors of isolated epithelial cells derived from a carcinoma line and developed a theoretical understanding of how their behaviors arise from molecular-level chirality. We first found that the nucleus rotates, and the cytoplasm circulates in a clockwise direction in a cell. During the rotation, actin and myosin IIA are organized into stress fibers with a vortex-like chiral orientation at the ventral side of the cell periphery, simultaneously forming thin filaments with a concentric orientation at the dorsal level of the cell. Lattice light-sheet microscopy showed that these concentric filaments moved in a clockwise direction, suggesting their potential involvement in the rotation of intracellular components. On the other hand, when stress fibers with chiral orientations were removed by drug treatment, cells still exhibited intracellular rotation, implying that the cells generate rotational force without any macroscopic cell-scale chiral orientational order of the cytoskeleton. To elucidate how concentric actomyosin filaments induce chiral rotation, we analyzed a hydrodynamic model considering the microscopic chirality of actomyosin filaments. Our experiments and theory suggest that cell chirality emerges driven by the microscopic chirality of actomyosin rather than the macroscopic chiral orientational order.

Significance statement Cell chirality, the fundamental asymmetry of cells, originates from molecular chirality, and plays a crucial role in establishing the left-right asymmetry of organs and tissues. Active torque induced by the cytoskeleton has been implicated in the mechanism behind cell chirality. However, the precise organization of molecular-scale torque driving cell chirality remains elusive. In our study, we observed a clockwise rotational motion of the nucleus and cytoplasm in singly isolated epithelial cells derived from a colorectal carcinoma line. Our investigation suggests that the non-chiral structure formed by actin and myosin II is responsible for driving cell chirality. Our theory, based on active hydrodynamics, further suggests that the concentric orientation of actomyosin induces the clockwise cytoplasmic flow.

INTRODUCTION

Left-right asymmetry is ubiquitously observed in the bodies and organs of organisms. Despite extensive research, however, we still do not have a complete understanding of how left-right asymmetric structures are formed at an organismal scale. The breaking of left-right symmetry at the body and organ scale has been investigated in embryonic bodies, such as early vertebrate embryo [1, 2] nematodes [3–5] and pond snails [6–8]; and in organogenesis, such as embryonic hindgut [9–11] and male genitalia [12] in *Drosophila* and heart-looping in the chicken [13]. Interestingly, in most of these cases, the left-right symmetry breaking at the organ scale is associated with chiral features at the cellular scale, indicating that cell-level chirality induces multicellular chirality [14]. Chiral dynamics have been observed in isolated single cells, such as nerve cells [15], zebrafish melanophores [16], human foreskin fibroblasts [17, 18], and Madin-Darby canine kidney (MDCK) cells [19]. Furthermore, experimental and theoretical studies have revealed that cell-intrinsic chirality drives left-right asymmetric morphogenesis of tissues [20–22] and organs [13]. Therefore, to elucidate the mechanism of left-right symmetry breaking of organismal structures, it is essential to comprehensively investigate the mechanism underlying chiral dynamics at the single-cell scale.

In cells, there are many chiral components, such as amino acids, proteins, and DNA, and their proper organization can induce chiral properties of cells [23]. Par-

* These two authors contributed equally
† To whom correspondence may be addressed: tatsuo.shibata@riken.jp

ticularly, cytoskeletal molecules such as actin and microtubules have been suggested as candidate apparatuses driving chiral dynamics at the single-cell scale. For instance, actin and myosin are responsible for the chiral nuclear rotation of zebrafish melanophore [16], and the chiral neurite extension in nerve cells [15]. Actin polymerization by formin drives chiral swirling of the cytoskeleton in human fibroblasts [17]. Microtubules are involved in the chirality of neutrophils [24]. These studies attribute the chiral cell dynamics to the chiral rotating dynamics of actin and microtubules driven by molecular motors [25, 26]. However, a mechanistic understanding of how these molecules generate cell-scale chirality is still not complete. Several attempts to gain mechanistic insights using theoretical models indicate that the chiral symmetry breaking at the cellular level requires spatial coordination of chiral cytoskeletal molecules [3, 17]. Therefore, to crack the code of cellular chirality, it is important to elucidate how molecular-scale chiral activity spatially coordinates to trigger cellular-scale chirality.

In the present study, we investigated the behavior of Caco2 cells, a typical epithelial cell line that was derived from colorectal adenocarcinoma. We found that, when these cells were singly isolated and cultured on substrates, the nucleus rotates along with the circulation of the cytoplasm in a clockwise direction, as viewed from above. We then showed that actin and myosin II are responsible for this rotation of intracellular components. These cytoskeletal molecules formed concentric actomyosin filaments at the dorsal side of the cells, while they were organized into stress fibers with a vortex-like chiral orientation at the ventral side. Our experiments suggest that the former structure most likely drives the rotating motion, implying that a cell can rotate without any cell-scale chiral orientational order of the cytoskeleton. To elucidate whether the concentric achiral pattern of the cytoskeleton can indeed generate rotational flow, we analyzed a hydrodynamic model, based on the active chiral fluid theory, of a three-dimensional (3D) cell, considering the effect of molecular chirality of actin and myosin. We found that the concentric achiral structure of actomyosin can generate chiral cytoplasmic circulation, due to the force which originates from the molecular chirality of individual cytoskeletal components, even without cell-scale chirality.

RESULTS

Nuclei of singly isolated Caco2 cells rotate in a clockwise direction

To study the rotational dynamics of epithelial cells, we cultured singly isolated Caco2 cells and imaged them using a differential interference contrast (DIC) microscope (Fig. 1A, Movie S1). 76% of isolated Caco2 cells spread circularly on a collagen-coated glass substrate, generating lamellipodia in all directions along the cell periphery with no persistent migration [27]. In these cells, we noticed that the nuclei exhibit rotational motion in a clockwise direction when viewed from the dorsal (apical) side (Fig. 1B). 24% of the cells exhibited migratory behavior at the start of our live imaging, and it took a while for the cells to spread circularly without persistent migration. The cells exhibiting migratory behavior were excluded from the analysis.

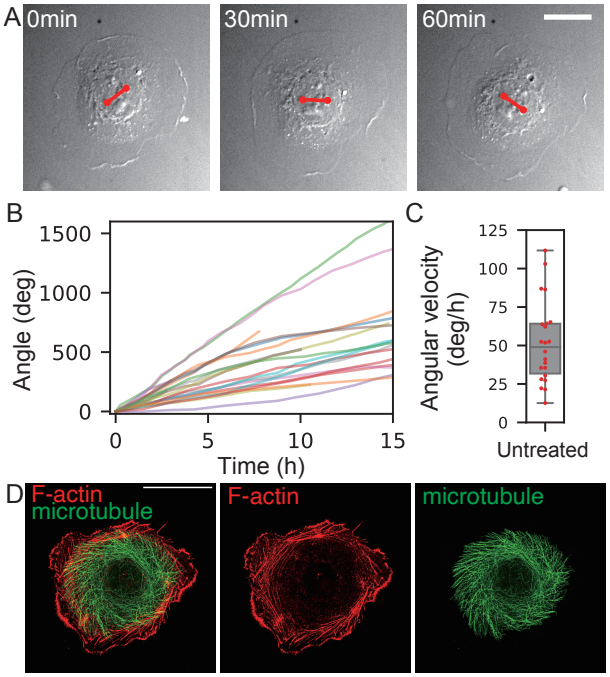

FIG. 1. Chiral nuclear rotation and cytoplasmic flow in singly isolated Caco2 cells. (A) Rotating nucleus probed by the rotation of nuclear texture. The endpoints of the red line segments are the positions of tracked landmarks of the nucleus. (B) The cumulative angle of nuclear rotation plotted against time and (C) average angular velocity ($n = 22$). Here, positive angle values indicate clockwise rotation. (D) Chiral cytoskeletal structure of F-actin (phalloidin) and microtubule (immunostaining). Scale bar: 20 µm.

The speed of nuclear rotation was about 50 degrees per hour on average (Fig. 1C). We measured the rotational speed by tracking unique points of the nuclear texture (Fig. 1A). The texture of the cytoplasm around the nucleus also showed a rotating motion, which indicates that the cytoplasm circulates in the same direction (Fig. 1A). Furthermore, we found that microbeads attached to the dorsal surface rotate (Movie S2), confirming that the dorsal membrane also rotates. The rotating motion of cells persists for more than eight hours until cell division occurs. After the cell division, cells form two-cell colonies, and then the nuclear rotation resumes. In this work, we focus on the rotating motion in singly isolated cells.

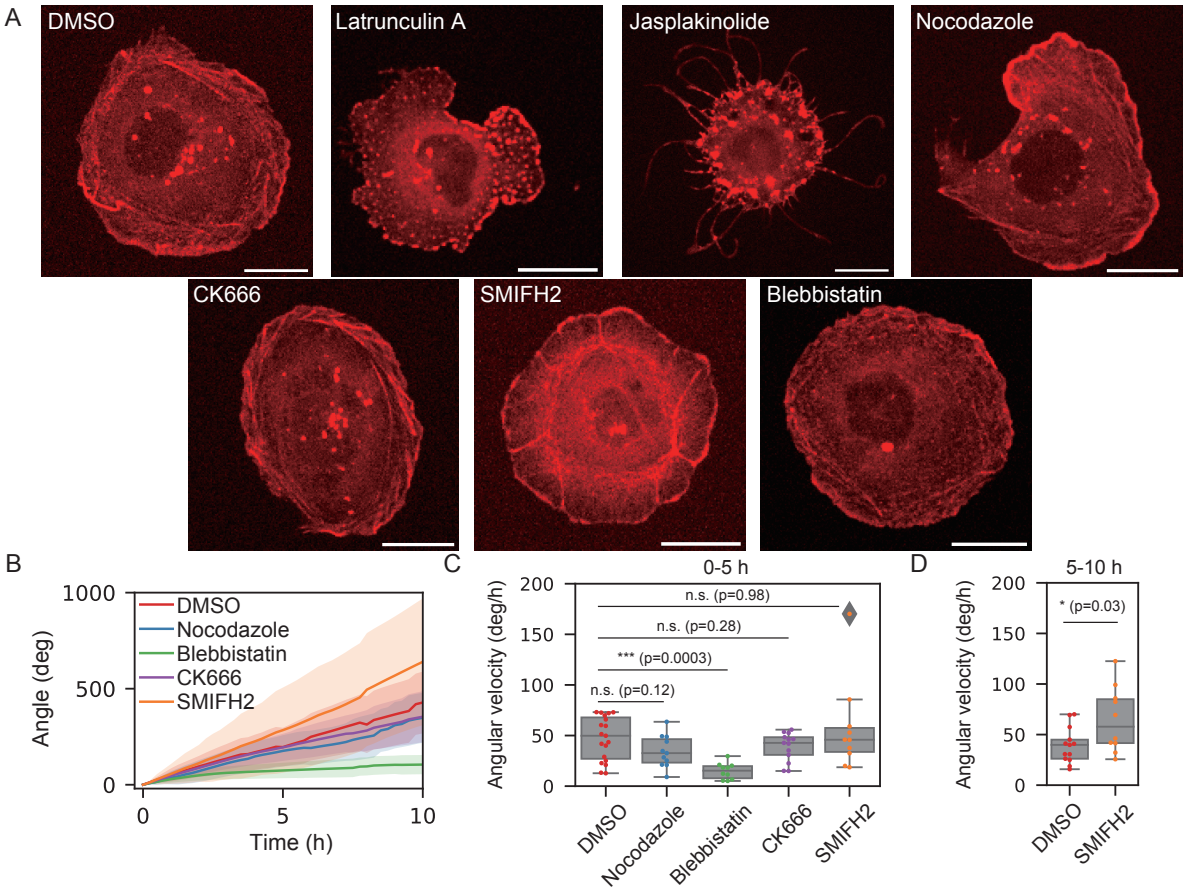

FIG. 2. Identification of molecular mechanisms responsible for the chiral rotation. Roles of F-actin, microtubule, Arp2/3, Formin-mediated actin polymerization, and myosin II activity were investigated: Cells were treated with DMSO (0.2%, control), actin polymerization inhibitor latrunculin A (2 µM), actin depolymerization inhibitor Jasplakinoilide (10 nM), microtubule inhibitor nocodazole (50 µM), myosin II inhibitor blebbistatin (1 µM), Arp2/3 inhibitor CK666 (200 µM), or formin inhibitor SMIFH2 (40 µM). (A) Snapshot images from the live image of actin dynamics in cells expressing Lifeact-RFP. Scale bar: 20 µm. (B) The cumulative angle of nuclear rotation averaged over different cells plotted against time for different conditions: DMSO ($n = 19$), nocodazole ($n = 11$), blebbistatin ($n = 10$), CK666 ($n = 13$), SMIFH2 ($n = 10$). The standard deviation is represented by shaded regions. (C) Angular velocity of cells under different conditions averaged over the first 5 hours of the time-evolution plot in (B). (D) Angular velocity of control and SMIFH2-treated cells averaged over the last 5 hours of the time-evolution plot in (B): DMSO ($n = 13$) and SMIFH2 ($n = 10$). p values were calculated using the Mann-Whitney-U test ($* : p < 0.05, ** : p < 0.01, *** : p < 0.001$). Here, positive angle values indicate clockwise rotation.

F-actin and microtubules exhibit chiral patterns

We hypothesized that cytoskeletal molecules, such as F-actin and microtubules, are responsible for the circulating flow. To see the structure and dynamics of actin, we imaged live Caco2 cells expressing Lifeact-RFP (Movie S1). Actin bundles in the peripheral region of cells were tilted to form a chiral pattern in a counterclockwise direction (Fig. 1D). Since each of these actin bundles associates with vinculin (Fig. S1), a focal adhesion protein, at their termini, we call them stress fibers [28]. We next studied how microtubules are organized in the cytoplasm during nuclear rotation. To this end, we visualized microtubules with the GFP-tagged microtubule-binding domain of ensconsin (EMTB-3XGFP [29]). Microtubules spread over the entire cytoplasmic region and exhibited a chiral pattern swirling in a clockwise direction (Movie S3). The swirling always occurs in a clockwise direction, as shown in Fig. 1D, consistent with the rotational direction of the nucleus. To summarize, actin bundles in the cell peripheral region and microtubules in the cytoplasm showed chiral patterns.

F-actin and myosin-II are indispensable for chiral rotation

To investigate whether the cytoskeletons with chiral patterns drive the circulating flow, we performed

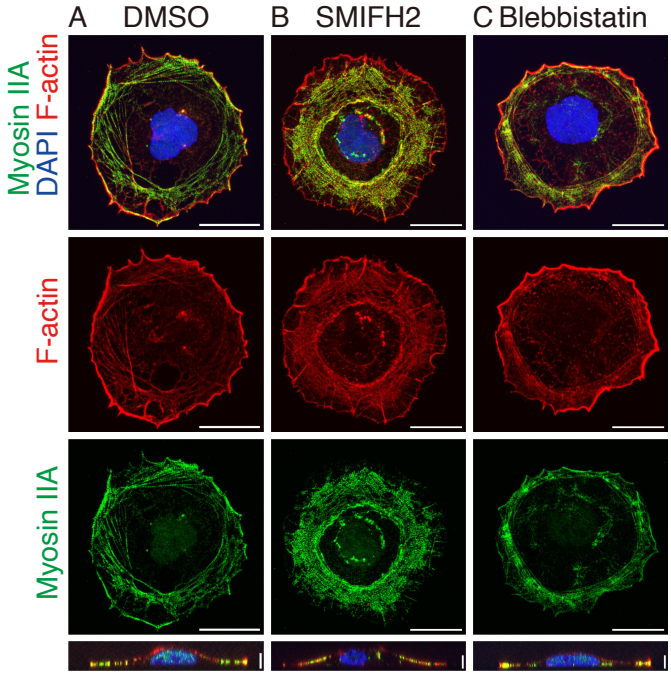

FIG. 3. Organization of F-actin and Myosin IIA. (A) Control cells treated with DMSO show a chiral tilted pattern of F-actin and myosin II visualized by phalloidin and immunofluorescence with an antibody against myosin IIA, respectively. (B) SMIFH2 (40 μM) treated cells show a concentric pattern of F-actin and myosin II. (C) The chiral tilted pattern of F-actin and myosin II is suppressed in cells treated with blebbistatin (1 μM). The bottom panel shows vertical cross sections. Scale bars: 20μm (horizontal) and 5μm (vertical).

live imaging of Caco2 cells expressing Lifeact-RFP with small-molecule inhibitors of cytoskeletal structures. When cells were treated with the actin polymerization inhibitor latrunculin A or F-actin stabilizer jasplakinolide, the shape of the cell periphery became rough and nuclear rotation stopped (Fig. 2A, Movies S4 and S5, respectively), indicating that F-actin is necessary for the nuclear and cytoplasmic rotation. In contrast, disruption of microtubules by nocodazole did not affect the nuclear rotation (Figs. 2A, B and C, Fig. S2 and Movie S6), which indicates that microtubules are not involved in the rotating motion.

To reveal which activities of actin are involved in the chiral rotating motion, we first investigated the role of Arp2/3- and formin-driven actin polymerization on the rotating motion, since a previous report has shown that they are involved in the chiral behavior of human foreskin fibroblasts [17]. When Caco2 cells were treated with the Arp2/3 complex inhibitor CK666 [30], lamellipodia at the cell periphery tended to shrink (Fig. 2A, Movie S7), but the nuclear rotation was maintained (Figs. 2B and C), indicating that lamellipodia formation mediated by the Arp2/3 complex was dispensable for the rotating motion.

When the cells were treated with SMIFH2 [31], chiral stress fibers mostly disappeared at the cell peripheral region, but instead, another pattern of F-actin appeared (Fig. 2A and Movie S8). To investigate the distribution of F-actin more closely, we performed immunostaining using phalloidin and imaged cells in 3D (Fig. 3). Figure 3B shows that a subset of actin bundles became oriented in a radial direction, unlike the chiral pattern of stress fiber originally observed in the control cells (Fig. 3A). Furthermore, another population of F-actin was organized into a dense network or cluster with a concentric pattern (Fig. 3B). Intriguingly, in spite of these drastic changes in the spatial organization of F-actin, the rotating motion was maintained (Figs. 2B and C). Therefore, we conclude that formin-driven actin polymerization is not responsible for the chiral rotational motion. Furthermore, as shown in Fig. 2D, we noticed that, while the rotating speeds of control and SMIFH2-treated cells were comparable in the first five hours of the observation window, the SMIFH2-treated cells rotated significantly faster than control cells, on average, in the second five hours: the rotating speed of control cells slightly decreased over time, while SMIFH2-treated cells maintained or even slightly accelerated the rotating speed (Figs. 2B-D), further suggesting that formin is not required but even inhibitory for the rotation mechanism being studied here.

In previous studies, it has been shown that the chirality in various cell types depends on the activity of myosin II. It has also been proposed that myosin II with F-actin generates chiral torque on a molecular scale [3, 32–34]. Therefore, we next investigated the role of myosin II in the chiral rotation by treating Caco2 cells with the myosin II inhibitor, blebbistatin. Under this condition, the chiral pattern of peripheral F-actin became less prominent (Fig. 3C and Movie S9), while the nuclear rotation was mostly suppressed (Figs. 2B and C). Therefore, the activity of myosin II seems to be required for the chiral rotational motion, and also for the formation of a chiral pattern of stress fibers. On the other hand, our aforementioned results indicated that peripheral stress fibers are not a critical component to drive the rotational motion, and therefore myosin II is thought to control other subcellular mechanisms. In summary, both the activities of F-actin and myosin II are important for nuclear and cytoplasmic rotation.

Super-resolution 3D imaging of actin and myosin-II

To further investigate the roles of F-actin and myosin II in the chiral rotation, we analyzed the distribution and dynamics of F-actin and myosin II in more detail, using control and SMIFH2-treated cells.

To this end, we performed a 3D super-resolution microscopy called expansion microscopy (ExM). We first observed the distribution of F-actin stained with phalloidin under control conditions (Fig. 4A). In the peripheral region of the cell, stress fibers showed a swirling pattern (orange in the left panel and bold lines in the right

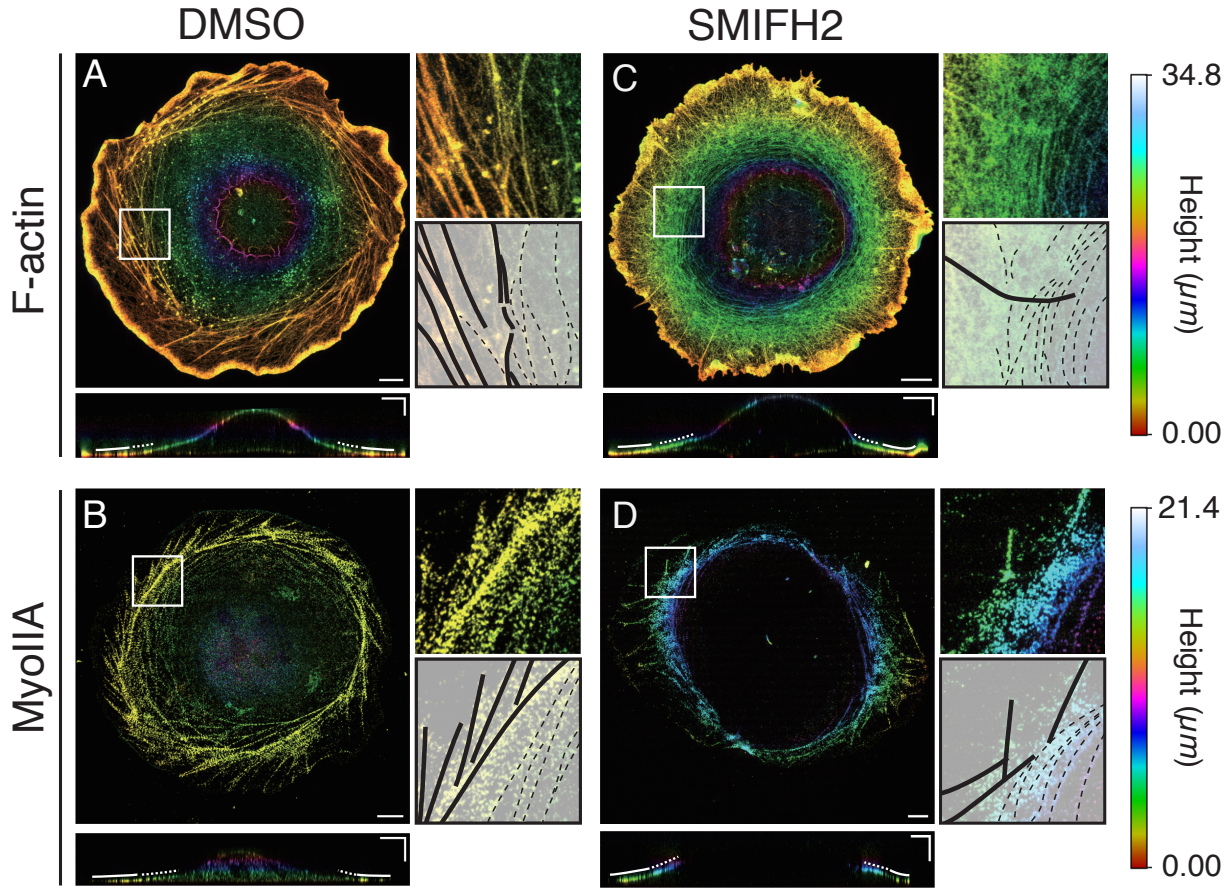

FIG. 4. ExM imaging of F-actin and myosin IIA. Maximum intensity projection (MIP) images of F-actin (A, C) and myosin IIA (B, D) in DMSO (A, B) and SMIFH2 (C, D) treated cells. The color indicates the height along the z-axis, where the height was measured after the samples were swollen (color bar, right). Magnified views of the white boxes are shown in the right top panels, and corresponding outlines of F-actin are shown in the right bottom panels, where the bold and dotted lines indicate thick and thin fibers, respectively. The vertical cross-sections (xz) are shown in the bottom panels, where the bold and dotted lines indicate the peripheral and dorsal inner regions, respectively. Scale bars: 20 µm (horizontal) and 10 µm (vertical).

panel of Fig. 4A; dark red line Fig. 5I left). Around the inner edge of the peripheral cytoplasmic zone having stress fibers, we detected another population of actin filaments, which are thinner than stress fibers, and do not exhibit obvious chiral orientation but are parallel to the tangential direction of the cell edge (green in the left panel and dotted lines in the right panel of Fig. 4A; light blue line in Fig. 5I left). In z-section images, (Fig. 4A bottom), these thin actin filaments are distributed along the dorsal membranes of the cell (green in Fig. 4A), unlike the stress fibers that are localized at the ventral side (orange in Fig. 4A). We also used antibodies to probe the distribution of myosin IIA (Fig. 4B). The distribution of myosin IIA is similar to that of F-actin, except for its striped pattern. Since we could not assess the colocalization of F-actin and myosin IIA filaments in the same cells in ExM due to a technical reason, we investigated their localization using conventional confocal microscopy (Fig. 3A and Movie S10). The confocal microscopy images indicate that F-actin and myosin IIA generally colocalize with one another in these specimens.

We next examined the distribution of F-actin and myosin II in the cells treated with SMIFH2 (Figs. 4C and D). As observed by conventional confocal microscopy, the chirally tilted actin stress fibers disappeared at the peripheral region, and instead thick F-actin bundles extended radially from the cell edge toward its center (bold line in Fig. 4C right; dark red line in Fig. 5I right). In the interior region, thin actin filaments were organized into a dense network with a concentric pattern (green in the left and dotted lines in the right panels in Fig. 4C; light blue line in Fig. 5I right). Notably, these concentric actin filaments were distributed at the dorsal side of cells (green in the bottom panel Fig. 4C). Myosin IIA exhibited a similar reorganization as seen in F-actin (Fig. 4D). As observed in control cells, confocal microscopy showed that F-actin and myosin IIA colocalize also in the SMIFH2-treated cells, particularly in the concentric actin clusters (Fig. 3B), confirming that non-stress fiber actin filaments also associate with myosin IIA. Thus, ExM analysis revealed more detailed feature of actomyosin distribution, particularly detecting thin actomyosin filaments

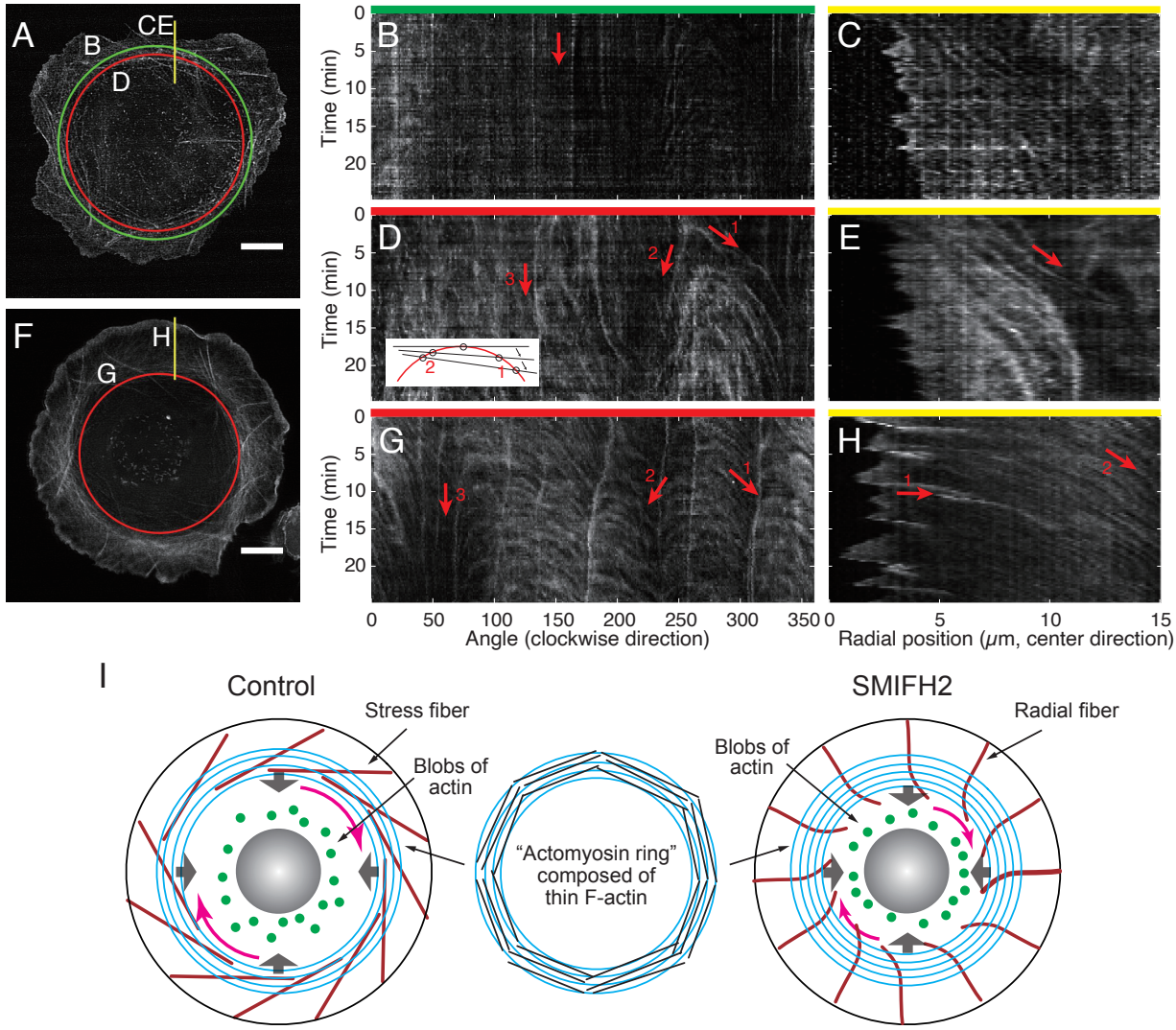

FIG. 5. Dynamics of F-actin in Caco2 cells live-imaged by lattice light-sheet microscopy (LLSM). (A) Maximum intensity projection (MIP) image of Caco2 treated with DMSO. (B) Kymograph along the green circle in (A), obtained from a slice at $z = 0$. $z = 0$ is defined as the plane closest to the substrate. (C) Kymograph along the yellow line in (A), obtained from a slice at $z = 0$. (D) Kymograph along the red circle in (A), obtained from a slice at $z = 0.5$ μm. inset: schematic diagram of F-actin (black lines) passing through the circle. (E) Kymograph along the yellow line in (A), obtained from a slice $z = 0.5$ μm. (F) MIP image of Caco2 treated with SMIFH2 (40 μM). (G) Kymograph along the red circle in (F), obtained from the MIP image. (H) Kymograph along the yellow line in (F), obtained from the MIP image. (I) Schematic diagram of F-actin structure in control and SMIFH2 treated cells. Thick stress fibers (dark red) were immobile, while the "actomyosin ring" (light blue), which consists of thin actin filaments, moved in centripetal and clockwise directions. Scale bar: 10 µm.

with a concentric orientation, located more inside the cell than the peripheral stress fibers. Additionally, we examined cells treated with blebbistatin by ExM, confirming the results obtained by the live imaging and the conventional immunostaining (Figs. 2A and 3C) that chiral stress fibers were greatly reduced after this treatment (Fig. S3).

F-actin consisting of the "actomyosin ring" flows

To gain further insights into the role of the actomyosin system in the mechanism of intracellular rotation, we examined how F-actin behaves during the rotational process. To this end, we performed live imaging of Caco2 cells expressing Lifeact-mEmerald, using lattice light-sheet microscopy (LLSM). Since LLSM has a higher spatial resolution particularly in the z-direction compared to conventional confocal microscopy, we could identify the dynamics of F-actin in 3D more precisely. Figures 5B-E show kymographs of F-actin dynamics along different

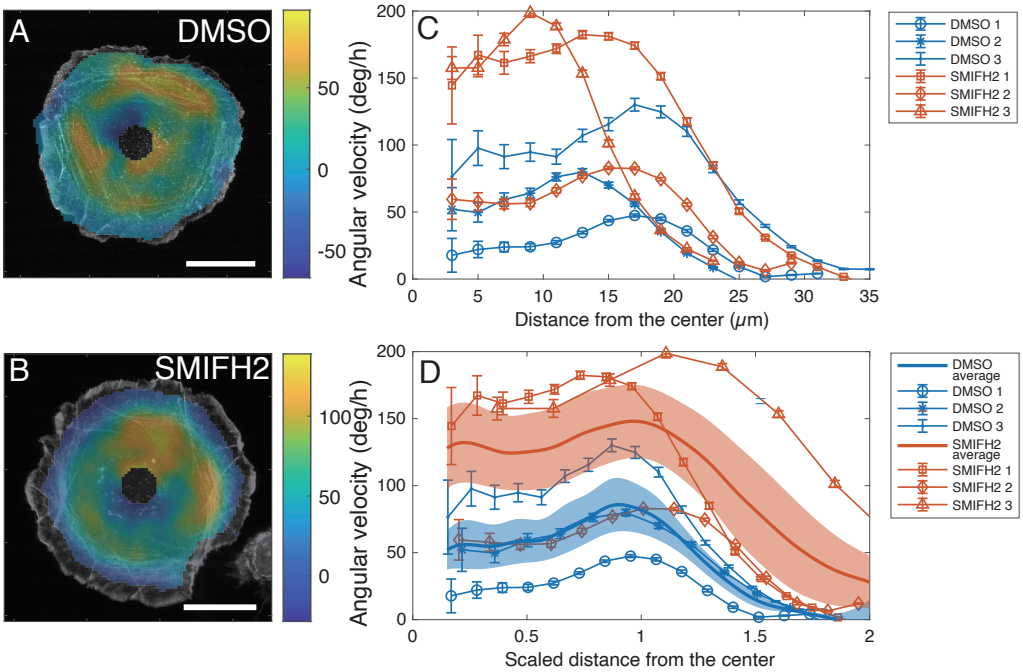

FIG. 6. Angular velocity obtained by the PIV analysis. (A-B) Spatial profile of angular velocity (color code) obtained from the time-average of the PIV vector filed in a control cell (A: DMSO) or in a cell treated with SMIFH2 (B) superimposed on a snapshot F-actin image. Scale bar: 20 µm. (C) Average angular velocity as a function of the distance from the center. (D) Average angular velocity as a function of a distance scaled by the inner radius of the actomyosin ring of individual cells. Here, positive angular velocity indicates clockwise rotation. Sample averages for two conditions are indicated by the solid lines. Error bars and shaded areas represent standard errors of the means (SEM).

lines, drawn in Fig. 5A, at different heights z in control cells. In Figs. 5B and C, the kymographs along the green circle and the yellow line, which were analyzed at the ventral side, indicate that F-actin bundles in the peripheral region with the chiral tilted pattern are immobile on more ventral sides (arrow in Fig. 5B, see also Movie S11). Figures 5D and E show the kymographs along the red circle and the yellow line (drawn in Fig. 5A), respectively, at the height where the dorsal cell membrane exists. Rightward descending lines in the kymograph along the red circle indicate that the filaments move in a clockwise direction (Fig. 5D, arrow 1). There are also leftward descending lines that appear at the same time as the rightward descending lines appear but with different steepness (Fig. 5D, arrow 2). These pairs of lines indicate that the filaments are moving in a clockwise direction, as well as centripetally (Fig. 5D inset). Furthermore, the kymograph along the yellow line (Fig. 5A) also indicates that the filaments are moving centripetally (Fig. 5E). To summarize, on the dorsal cell membrane, actin filaments, which are concentrically distributed, move in a clockwise direction while also moving in a radial direction (see also Movie S11): we hereafter call this concentric structure "the actomyosin ring" (Fig. 5I).

To see if the actomyosin ring is involved in driving the rotating flow, we inferred the spatial distribution of flow speed and orientation (velocity field) from the F-actin time-lapse images using particle image velocimetry (PIV) (Figs. 6, S4, and Movie S13). In the cytoplasmic region between the actomyosin ring and the nucleus, we did not detect clear actin filaments, but only found blobs of actin (Fig. 5A, and green dots in Fig. 5I). These blobs also circulate in a clockwise direction. From the velocity field inside the cells inferred by PIV, we calculated the angular component of the velocity with respect to the cell center and then converted it into the angular velocity, i.e. change in the angle per unit time. The spatial profile of the angular velocity (Fig. 6A and Figs. S4A-C) indicates that it is higher in the region where F-actin accumulates, rather than the region where the actin blobs are present, indicating that the driving force could be present in the region of the actomyosin ring.

The angular velocity averaged over the angular direction was then plotted along the radial direction for control cells (Fig. 6C) and the peaks were found in the range from 10 to 20 µm. Since the size of the actomyosin ring varies from cell to cell, we manually determined the region of the actomyosin ring, and then replotted the angular velocity against the distance scaled by the inner radius of the actomyosin ring (Fig. 6D). We found that the peak positions locate around the scaled distance of one, which suggests that the driving force is present in the region around the actomyosin ring.

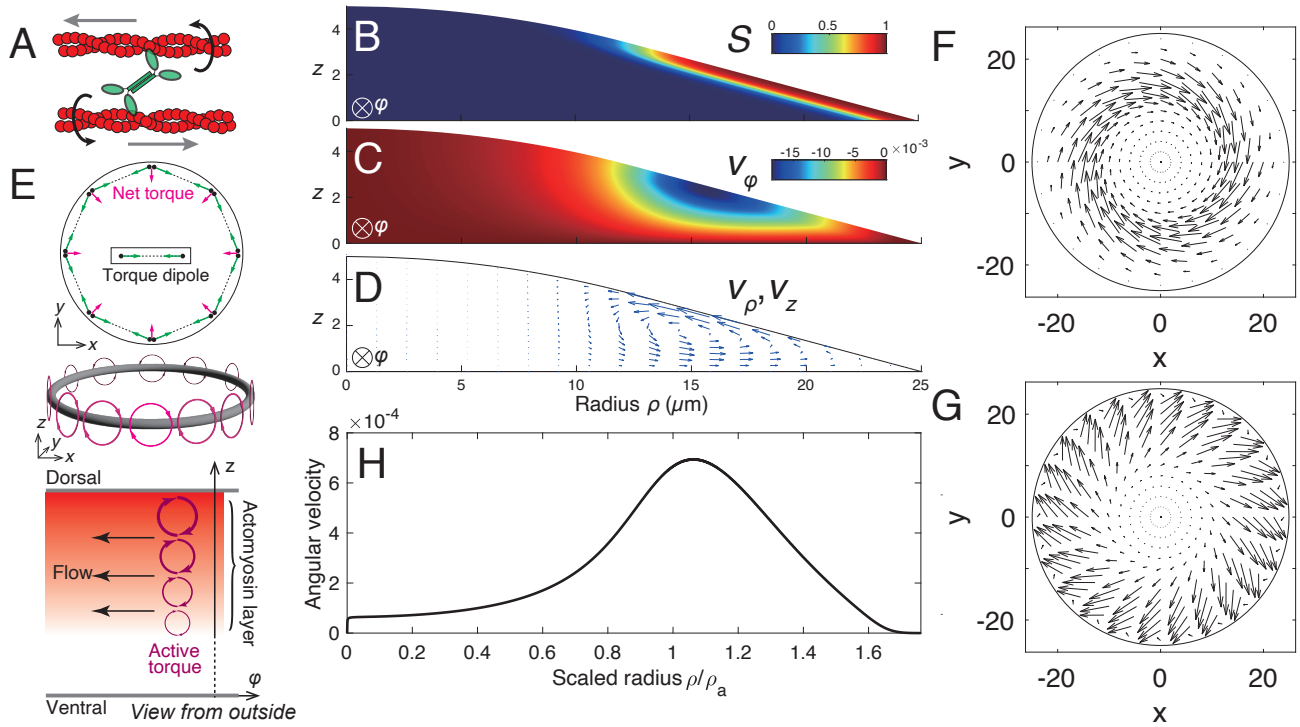

FIG. 7. Theoretical model for the chiral cytoplasmic flow. (A) Actomyosin generates a force dipole and a torque dipole. (B-D) Numerical simulation of Eq. 1 assuming that the cell shape is axisymmetric around the cell center. (B) Actomyosin is distributed along the dorsal membrane with a concentric orientation. (C) Azimuthal velocity v_φ showing negative values indicating that the flow is generated in a clockwise direction. (D) Velocity in the radial ρ- and z- directions, (v_ρ, v_z), indicated by vectors. Circulating flow is generated in the ρ-z plane. (E) Top: A concentric orientational field on a ring generates net torque in the center direction (magenta arrow). Middle: Active torque (magenta clockwise arrow) generated by a concentric orientational field on a ring. Bottom: A gradient of active torque (magenta clockwise arrow) in the z direction, resulting in a rotational flow clockwise (black arrow). (F) Flow profile along the dorsal side showing an inward swirling pattern in a clockwise direction. (G) Flow profile at the ventral side showing an outward swirling pattern in a counterclockwise direction. (H) Angular velocity averaged in the z direction plotted along the radial direction, showing a peak at around $\rho/\rho_a = 1$. Here, ρ_a is the leftmost position where $S \geq 0.8$.

Actomyosin ring flows in SMIFH2-treated cells

We also examined the dynamics of actin bundles in cells treated with SMIFH2, using live image data obtained by LLSM (Figs. 5F-H). In Figs. 5G and H, the kymographs along the red circle and yellow line (drawn in Fig. 5F), respectively, indicate that the entire actin clusters forming a concentric pattern move in a clockwise direction (Fig. 5G), and simultaneously flow centripetally (Fig. 5H), similar to the control condition. Additionally, we found that in contrast to the immobile stress fibers with a chiral pattern in control cells (dark red line in Fig. 5I left), F-actin bundles radially extending from the cell periphery in SMIFH2-treated cells tended to move in a clockwise direction at their proximal ends, although they seem to keep the anchorage of the distal ends to the cell edge (Fig. 5B, see also Movie S12 and dark red line in Fig. 5I right), suggesting that the nature of peripheral F-actin was also altered. Thus, the concentric ring of flowing thin actin filaments was detected also in the SMIFH2-treated cells, but showed modified features (Fig. 5I). Importantly, it seems that the ring developed more extensively after SMIFH2 treatment.

As in the control cells, the angular velocity inferred by PIV was high at the region around the inner edge of the actomyosin ring (Figs. 6B-D), which indicates that the driving force of the circulating flow is located in the region of the actomyosin ring like the control cells.

We additionally observed another interesting phenomenon to support our idea. In a SMIFH2-treated cell that was imaged by a conventional fluorescent confocal microscope (LSM880, Zeiss), we, by chance, observed that fluorescent debris that seemed to attach to the actomyosin ring persistently circulated approximately three times as fast as the rotating speed of the nucleus: ~ 400 degree/hour and ~ 140 degree/hour for the debris and nucleus, respectively. (Movie S14, yellow and white lines, respectively). In the other cell observed by LLSM, we observed two fluorescent debris circulating in the area of the actomyosin ring, and in the cytoplasmic region between the actomyosin ring and the nucleus (Movie S15, yellow and red circles): the angular velocities of the circulating

debris were ~ 250 degree/hour and ~ 190 degree/hour, respectively. Although we could not measure the rotating speed of the nucleus in the second cell because the nucleus was barely visible in the LLSM live image, the circulating speeds of the debris are more than two times faster than the typical nuclear angular velocity of SMIFH2-treated cells (Figs. 2B-D). These observations support that the actomyosin ring generates a driving force for rotating the nucleus and cytoplasm. Note, since the angular velocity estimated from the motion of debris was faster than that obtained from the PIV analysis, our PIV analysis for F-actin dynamics may underestimate the flow velocity.

In order to investigate the effects of SMIFH2 treatment on the rotational dynamics, we compared the angular velocity profiles inferred from the PIV between control and SMIFH2-treated cells. As shown in Fig. 6D, the angular velocity profiles averaged over samples indicate that the SMIFH2-treated cells tended to exhibit a faster speed compared to the control cells. This finding is consistent with the observation that SMIFH2-treated cells tended to exhibit a faster nuclear rotation, as shown in Fig. 2D.

A theoretical model of chiral cytoplasmic flow induced by the actomyosin ring

Our experimental observations indicate the possibility that the actomyosin ring is a cell-scale structure that drives the chiral cytoplasmic flow. Previous studies reported that chiral cytoplasmic flows are driven by the chiral macroscopic cell-scale order of F-actin [35]. However, in contrast to previous studies, the actomyosin ring we observed has a concentric pattern and does not show an obvious macroscopic chiral structure. We here theoretically address how such an achiral concentric pattern can drive the chiral circulating flow.

We employ a theoretical framework of active chiral fluid [3, 32, 33], which has been proposed to describe the fluid dynamics driven by active chiral components. We model the actomyosin ring as an active chiral fluid driven by two active elements: 1) a force dipole originating from the contraction force of actomyosin and 2) a torque dipole generated when a bipolar myosin II filament rotates two antiparallel actin filaments to create a pair of counter-rotating vortex flows (Fig. 7A). By representing the orientation of actomyosin fibers as orientational field $\mathbf{p}$ and the fluid velocity as $\mathbf{v}$, the hydrodynamic equation is described by the Stokes equation with the active contributions:

$$0 = -\nabla P + \eta \nabla^2 \mathbf{v} + \zeta^a \nabla \cdot \mathbf{pp} + \frac{1}{2}\zeta^c \nabla \times (\nabla \cdot \mathbf{pp}), \quad (1)$$

where P is the pressure satisfying the incompressibility condition $\nabla \cdot \mathbf{v} = 0$ and η is the fluid viscosity. Here, the terms with ζ^a and ζ^c are forces generated by the force dipoles (achiral) and torque dipoles (chiral), respectively. ζ^a and ζ^c represent the strength of the forces. Considering that the actomyosin generates contractile force and torque as shown in Fig. 7A, the signs of the coefficients are $\zeta^a > 0$ and $\zeta^c > 0$. We hereafter assume $\zeta^a > 0$ and $\zeta^c > 0$, constant in space. We also assume the actomyosin filaments have a dipolar structure (Fig. 7A) so that Eq. 1 is invariant under $\mathbf{p} \to -\mathbf{p}$. We, for convenience, represent the spatial variation of the density and order of the actomyosin by introducing an effective order parameter S as $\mathbf{p} = S\mathbf{n}$ (see Eq. 9), where $\mathbf{n}$ is a unit vector.

We first numerically solved Eq. 1, assuming a cell with an axisymmetric geometry shown in Fig. S5. Based on experimental observation, we also assumed that actomyosin is distributed on the dorsal side, where the effective order parameter S is set to be positive reflecting the density distribution of actomyosin (Fig. 7B). Figure 7C shows the spatial profile of the azimuthal velocity v_φ in the vertical section of the cell. In the entire region, v_φ is negative, indicating that the flow is generated in a clockwise direction viewed from above. Thus, the numerical result shows that the concentric pattern of actomyosin can generate chiral cytoplasmic flow, and the direction is clockwise, consistent with our experimental observation.

How can we understand the underlying mechanism behind the chiral cytoplasmic flow resulting from the concentric pattern of actomyosin? The active chiral term $\zeta^c \nabla \times \nabla \cdot \mathbf{pp}$ in Eq. 1 can be interpreted as follows: the rotation of the axial vector field $\zeta^c \nabla \cdot \mathbf{pp}$, which is an active torque induced by chiral torque dipole, generates a force to induce a flow. For a concentric orientational field on a ring domain, the active torque $\zeta^c \nabla \cdot \mathbf{pp}$ is generated as shown in Fig. 7E top. The actomyosin ring formed along the dorsal side in Caco2 cells is regarded as a stack of concentric orientational fields on a ring. In the region where actomyosin is present ($S > 0$), the concentration of actomyosin naturally increases with z which leads to an increase of the effective order parameter S with respect to z as indicated in Fig. 7B. For such an orientational field, the strength of the active torque increases as the height z increases (Fig. 7E bottom), forming a gradient of the active torque strength in the z direction. Consequently, the gradient generates a force in a clockwise direction as viewed from above (Fig. 7E bottom black arrow, see also the right-hand side of Eq. 10).

In the numerical simulation, we also investigated the spatial profile of ρ and z components (v_ρ, v_z) of the velocity field. Figure 7D shows that inward flow to the cell center occurs on the dorsal side, while the flow in the opposite direction occurs on the ventral side, resulting in the circulating flow in the ρ-z plane (Fig. 7D). This circulating flow is driven by the contractile force dipole of actomyosin on the dorsal side. Due to the circulating flow in the ρ-z plane and the azimuthal flow, swirling flows appear on both dorsal and ventral sides (Figs. 7F and G, respectively). Interestingly, the tilting direction of the flow pattern on the ventral side is consistent with the chiral pattern of the stress fibers on the ventral side (Fig. 1D). This may imply that the chiral pattern of the stress fibers is self-organized through alignment with the

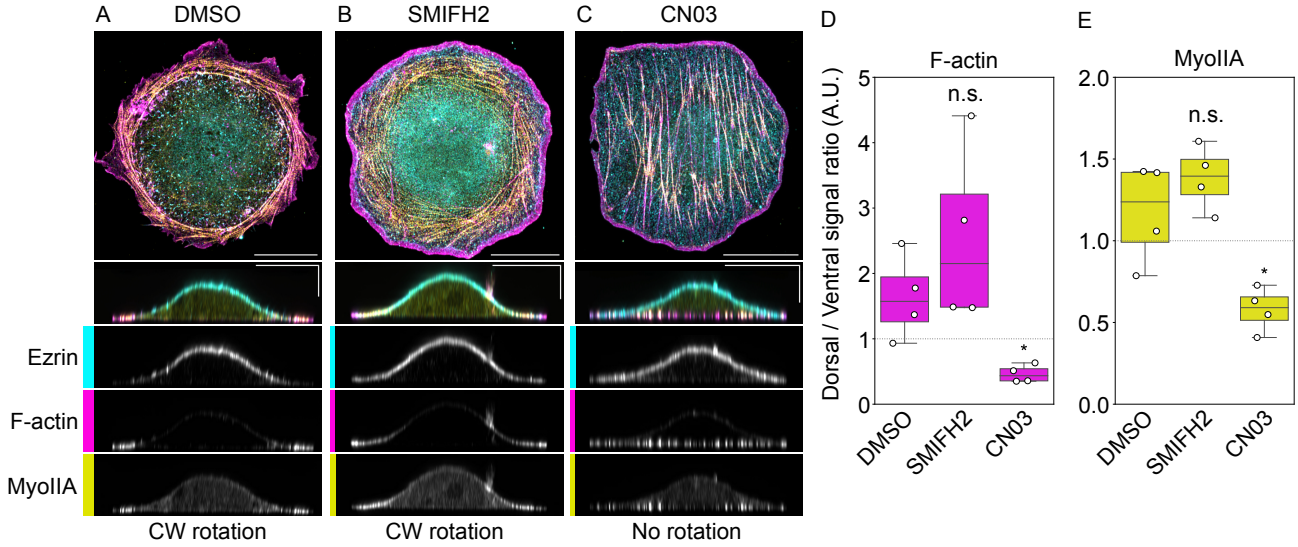

FIG. 8. Depletion of dorsal actin and myosin by Rho activator II stops the rotating motion of nucleus. (A) Actin (magenta) and myosin II (yellow) showing localization with the dorsal marker Ezrin (cyan) in the DMSO treated cell. (B) SMIFH2-treated cell showing an increase in dorsal actomyosin and a decrease in ventral actomyosin. (C) Rho Activator II (CN03) treated cell showing a decrease in dorsal actomyosin and an increase in ventral actomyosin. Control (DMSO) and SMIFH2-treated cells showed clockwise (CW) rotation, while CN03-treated cells did show rotation. Scale bars: 20 µm (horizontal) and 5 µm (vertical). (D, E) Ratio of dorsal F-actin (D) and MyoII (E) to the ventral ones. p values were calculated using the Mann-Whitney-U test. $*: p < 0.05$, n.s.: $p \geqq 0.05$.

fluid flow on the ventral side.

Furthermore, we analyzed the radial distribution of the angular velocity and found that it exhibits a peak around the inner edge of the actomyosin ring $\rho \sim \rho_a$ (Fig. 7H), consistent with the PIV analysis of the experimental data (Figs. 6C and D). ρ_a is the inner radius of the actomyosin ring determined by the threshold $S \geq 0.8$. This result further supports the idea that the actomyosin ring drives the rotation of the nucleus.

Depletion of dorsal actin and myosin stops the nuclear rotation

Our experimental observations and theoretical results suggest that the actomyosin ring located at the dorsal side of Caco2 cells plays a key role in the rotating motion. To further investigate this, we tested whether depletion of actomyosin at the dorsal side affected rotational motion. A previous study showed that the activation of RhoA by Rho Activator II (CN03), a specific RhoA activator, resulted in a decrease in apical stress fibers and an increase in basal stress fibers in vascular smooth muscle cells [36]. Based on this information, we aimed to decrease the ratio of the actomyosin at the dorsal to ventral sides in Caco2 cells using Rho Activator II. Remarkably, we observed a substantial increase in the thickness and number of actomyosin bundles at the ventral side, particularly beneath the nucleus, in Caco2 cells treated with Rho Activator II, while the dorsal actomyosin appeared to decrease significantly (Figs. 8 A and C). The ratio of dorsal to ventral actomyosin was reduced significantly in the cell treated with Rho Activator II compared with control cells (Figs. 8 D and E). We then performed live imaging of Caco2 cells treated with Rho activator II and found that the rotational motion of the nucleus ceased (Movie S16), supporting the idea that the dorsal actomyosin is crucial for driving the rotation. We also noticed that in cells treated with Rho activator II, the bundle of thick stress fibers was rearranged into a chordal pattern (Fig. 8C), and exhibited chiral motion (Movie S16), the mechanism of which remains to be understood. On the other hand, in cells treated with SMIFH2, the dorsal actomyosin appeared to increase, while the ventral actomyosin decreased (Figs. 8 A and B). The ratio of dorsal to ventral actomyosin in cells treated with SMIFH2 tended to increase although the difference was not statistically significant (Figs. 8 D and E). Taken together, our findings further support the idea that actomyosin at the dorsal side is crucial for driving rotation in Caco2 cells.

DISCUSSION

In this study, we investigated the mechanism underlying cell-scale chiral dynamics, which is observed in a Caco2 human epithelial cell when cultured as a single cell. We found that Caco2 cells exhibit nuclear rotation and cytoplasmic circulation, and the dynamics require actin and myosin II. High-resolution microscopy has revealed that the concentric actomyosin ring located on the dorsal side of the cells moves in a chiral fashion, leading us to

hypothesize that this process may play a critical role in driving cytoplasmic flow. To test this idea, we employed active chiral fluid theory [3, 32, 33]. Our theoretical analysis showed that the actomyosin localized at the dorsal membrane induces an active unidirectional fluid flow of the viscous cytoplasm and in turn nuclear rotation. Since the concentric pattern of actomyosin has no chirality at the cellular-scale, our theory indicates that the rotation of Caco2 cells is driven by the molecular-scale chiral mechanics of actomyosin rather than the cell-scale chiral orientation of actomyosin. It is also of note that we did not detect any visible cytoskeletal linkage between the nucleus and other cellular structures, another potential machinery for driving nuclear rotation. The nuclear rotation may be induced directly by the cytoplasmic circulating flow mediated by the friction between the nuclear surface and the cytoplasm.

Our experiments using inhibitors have revealed that myosin II is involved in the chirality of Caco2 cells. Previous studies have also shown that myosin II is involved in the chiral behaviors of several types of cells [35], while some of these studies concluded that formins are essential for breaking the chiral symmetry [7, 8, 17, 37, 38]. In contrast, our results showed that the rotational speed of Caco2 does not decrease but even slightly increases when treated with SMIFH2, a known inhibitor of formins, suggesting that formins may not be involved at least in the chiral symmetry breaking of Caco2 cells. We theoretically showed that the torque force generated by actin and myosin II is sufficient to explain the rotational motion. However, further experiments such as single-molecule live imaging of actin, myosin, and formin will be required to see if the rotation is fully understood by the mechanism we proposed.

In cells treated with SMIFH2, the actomyosin ring became more visible than in the control cells (Figs. 3, 4 and 8). This change may be attributable to the reduction in the formin activity by the administration of SMIFH2. The reduction in formin activity could have caused a decrease in the formation of stress fibers on the ventral side, followed by a shift of free actin and myosin II to the dorsal side, which may lead to the increase in the formation of actomyosin ring at the dorsal side. This consideration gives support for the model that dorsal actomyosin constituted the driving force behind the rotational motion, as the rotation tended to increase in SMIFH2-treated cells.

In a previous study [35], an achiral active fluid model was proposed to explain the rotation of the nucleus driven by actomyosin. In the theory, the concentric orientational order of actomyosin becomes unstable due to the spontaneous chiral symmetry breaking induced by the contractility of actomyosin, and then a chiral orientational order emerges to drive a unidirectional fluid flow to rotate the nucleus. Since there is no intrinsic chirality in the model, either clockwise or counter-clockwise rotation is selected with the equal probability. In contrast, in our theoretical model, we considered the intrinsic chirality of the actomyosin gel in order to explain our experiments where the rotational direction is always clockwise. Although our model is consistent with our experimental observations, there is still a limitation. We assumed a concentric orientational order of actomyosin. However, it remains to be elucidated how the concentric order is formed [39, 40], and how stable the structure is when the actomyosin has intrinsic chirality.

Several types of cells have been reported to exhibit chiral nuclear rotation. In particular, zebrafish melanophores show counterclockwise nuclear rotation [16], while singly isolated MDCK cells exhibited nuclear rotation in either direction with a bias to the counterclockwise direction [19]. Whether there is a common principle behind the chiral nuclear rotation or whether they are caused by different mechanisms remains to be clarified in future studies.

It has been suggested that the left-right asymmetry at the tissue level originates from chirality at the cellular level. However, it remains unclear how cell chirality coordinates to induce left-right asymmetry in multicellular organisms. Our previous theoretical studies showed that a tissue-scale asymmetry, such as a spatial gradient in the strength of cell-scale torque generation, is necessary for the tissue-scale left-right asymmetry to arise from cell chirality [12, 21, 22]. Hence, it will be necessary to investigate how cell chirality and tissue-level asymmetry coordinate to understand left-right asymmetry in organs and the body. Caco2 is an epithelial line, which can form multicellular layers. We thus hope that investigating the coordination between cell chirality and tissue-level chirality using cells, such as Caco2, which exhibit a clear individual chirality, is a promising approach to reveal the principles of chiral morphogenesis.

MATERIALS AND METHODS

Cell cultures and transfection

Caco2 cells were cultured in DMEM/Ham's F-12 (FUJIFILM Wako Pure Chemical Corporation, 048-29785) supplemented with 10% fetal bovine serum (SIGMA, F7524, Lot. BCBV 4600) and 1% penicillin/streptomycin (nacalai, 26253-84) at 37°C, 5% CO2 on collagen type I coated Dish (60 mm, IWAKI, 4010-010). For live-imaging of actin, we used Lifeact-RFP-transfected Caco2 cells which were established from Caco2 (ATCC) in [27]. To live-image the microtubule dynamics, we transiently transfected Caco2 cells with EMTB-3XGFP using Lipofectamine LTX Reagent with PLUS Reagent (Invitrogen, 15338100), according to the manufacturer's protocol. EMTB-3XGFP was a gift from William Bement [29] (Addgene plasmid # 26741 ; http://n2t.net/addgene:26741 ; RRID:Addgene_26741) For Lifeact-mEmerald (pLVSIN-EF1a-Lifeact-mEmerald-IRES-pur), mEmerald-Lifeact-7 was inserted into pLVSIN-EF1a-IRES-pur at the

BamHI and NotI sites by In-Fusion. The construction of pLVSIN-EF1a-IRES-pur has been described previously [41]. mEmerald-Lifeact-7 was a gift from Michael Davidson (Addgene plasmid # 54148 ; http://n2t.net/addgene:54148 ; RRID:Addgene_54148)

Live cell imaging

For live-image data in Figs. 1 and 2, we used an inverted fluorescence microscope (Olympus, IX-81) equipped with a spinning disk confocal imaging unit (Yokogawa, CSU-X1), a 60x/1.35 oil immersion objective (Olympus, UPLSAPO60XO), and a 561 nm laser (Coherent, Sapphire LP) for RFP excitation or a 488 nm laser (Coherent, Sapphire LP) for GFP excitation. We used a 40×/1.35 oil-immersion objective (Olympus, UApo/340) for the microtubule snapshots in Fig. S2. The cells were seeded sparsely on a collagen type I coated glass-based dish (IWAKI, 4970-011), and incubated in a stage-top incubator (Tokai Hit) at 37°C with 5% CO2 during live-imaging.

We took fluorescence images with multiple z-stacks (number of slices: 7 and Δz: 0.5 μm) by EMCCD (Andor Technology, iXon+) every 15 min, and then made maximum intensity Z projections. For the microtubule snapshots in Fig. S2, we applied a different condition (number of slices: 5 and Δz: 1 μm).

For the inhibitor experiments, the following inhibitors were used: latranculin A (SIGMA, L5163-100UG); Jasplakinolide (Toronto Research Chemicals Inc, J210700); Nocodazole (SIGMA-Aldrich, M1404); CK666 (SIGMA-Aldrich, SML0006-5MG); SMIFH2 (Wako, 4401/10); Blebbistatin (SIGMA, B0560-1MG); Rho Activator II (Cytoskeleton, Inc., Cat. #CN03, Lot # 025). We started live-imaging about 2-3 hours after seeding cells, and added the inhibitors about 40 min before the live-imaging.

When we observed the dynamics of the beads attached to the dorsal membrane of the cells, we used 2 μm carboxylate-modified beads (Invitrogen, F8887), and live-imaged the dynamics using the DIC channel of the microscope (Olympus, IX-81).

Analysis of cell rotation

We quantified the rotational behaviors of cells by manually tracking the dynamics of two nucleoli of each cell on DIC images (Segmentation Editor, Fiji). We defined the rotational angle of the cell by that of the line connecting the two nucleoli, and analyzed the rotational dynamics using Python. In Figs. 1A and B, we defined the initial time point of the measurement of the nuclear rotation by the time when we started the live-imaging. In the inhibitor experiments in Fig. 2, we determined the initial time point of the measurement as the time 5 hours after the initiation of live-imaging, accounting for the time lag needed for the inhibitors to exert their effects.

Immunofluorescence antibody staining and microscopy

Cells were seeded on collagen type I coated cover slips (Neuvitro Corporation, NEU-H-12-COLLAGEN-45) and treated with the inhibitors. After 8 hours, the cells were fixed with 2% PFA in PBS(-) for 10 min, permeabilized with 0.25% Triton X-100 in PBS(-) for 10 min, blocked with 3% BSA in PBS(-) for 30min. Then, we incubated cells with primary antibodies (2 hours), secondary antibodies (1 hour) and phalloidin (30 min) in a blocking buffer (3% BSA in PBS(-)). After washing with PBS(-) three times, the samples were mounted with a mounting medium with DAPI (Vector Laboratories, VECTASHIELD, H-1200). All the processes were performed at room temperature.

We used rabbit anti-Myosin IIA (Sigma-Aldrich, M8064, 1:1000 for IF), mouse anti-Vinculin (Sigma, V9131, 1:200 for IF), and mouse anti-Ezrin (Abcam, ab4069, 1:1000 for IF) as the primary antibodies and Alexa Fluor 488 goat anti-rabbit IgG (Sigma-Aldrich, 11034, 1:1000 for IF), Alexa Fluor 488 goat anti-mouse IgG (Invitrogen, A11029, 1:1000 for IF), and Alexa Fluor 647 donkey anti-mouse IgG (Sigma-Aldrich, AP192SA6, 1:1000 for IF) as the secondary antibodies, respectively. For actin staining, we used Alexa Fluor 568 phalloidin (Invitrogen, A12380, 1:400).

To analyze the sample, we took fluorescence images with multiple z-stacks (Δz: 0.32 μm) using a laser scanning confocal microscope (Zeiss, LSM880) equipped with Plan-Apochromat 63x/1.4 Oil DIC M27. Images were processed with Fiji.

Expansion Microscopy

Protein-retention Expansion Microscopy (ExM) was carried out as described previously [42]. Cells were cultured on collagen type I (SIGMA, C8919-20ML) coated cover slips and treated with the inhibitors. Fixation, permeabilization and blocking were performed as described above. To visualize F-actin, the cells were stained with Alexa Fluor 488 phalloidin (Invitrogen, A12379, 1:400) and next stained for 60 min with a rabbit anti-Alexa Fluor 488 antibody (abcam, ab150077, 1:500) as the primary antibody and Alexa Fluor 488-conjugated goat anti-rabbit (1:1000) as the secondary antibody [43]. After washing, cells were incubated with 100 μg/mL of 6-((Acryloyl)amino)hexanoic acid, succinimidyl ester overnight at room temperature in the dark. Samples were incubated in gelation solution (8.6% (w/w) sodium acrylate, 2.5% (w/w) acrylamide, 0.15% (w/w) N,N'-methylenebisacrylamide, 2 M NaCl, 1 x PBS, 0.1% TEMED, 0.1% ammonium persulfate) for 5 min on ice.

Gelation was allowed to proceed at room temperature for 1 hour. The gel and a cover slip were removed with tweezers and incubated with digestion buffer (0.5% Triton X-100, 1 x TE buffer, 1 M NaCl, 8 unit/mL Proteinase K) overnight at room temperature in the dark. The gels were removed from the digestion buffer and placed in 50 mL of Milli-Q water. Water was exchanged three times every 30 minutes. Most of the gels expanded to about 4.5 times their original size. Gels were placed on a poly-L-lysine (Sigma-Aldrich, P4707) coated glass bottom dish, and fluorescence images were taken by a laser scanning confocal microscope (Zeiss, LSM880).

Lattice Light Sheet Microscopy (LLSM) and image processing

The LLSM was home-built in the Kiyosue laboratory at RIKEN Center for Biosystems Dynamics Research following the design of the Betzig laboratory [44] under a research license agreement from Howard Hughes Medical Institute. Electric wiring was performed at RIKEN Advanced Manufacturing Support Team. Metal Parts were processed by Maeda Precision Manufacturing Ltd. and Zera Development Co. To create a lattice light sheet, a dithered square lattice was used through a spatial light modulator (Fourth Dimension Displays) in combination with an annular mask with 0.55 out and 0.44 inner numerical apertures (Photo-Sciences) and a custom NA 0.65 excitation objective (Special Optics). Images were acquired through a CFI Apo LWD 25XW 1.1-NA detection objective (Nikon) and a scientific sCMOS camera, Orca Flash 4.0 v3 (Hamamatsu Photonics). Caco2 cells expressing Lifeact-mEmerald were seeded on a collagen-coated coverslip 3h before imaging. During imaging, cells were maintained in DMEM/Ham's F-12 (FUJIFILM Wako Pure Chemical Corporation, 048-29785) supplemented with 10% fetal bovine serum (SIGMA, F7524, Lot. BCBV 4600) at 37°C, 5% CO2. For live imaging of Lifeact-mEmerald, a 488-nm laser (MPB Communications) and a long-pass emission filter BLP01-488R-25 (Semrock) were used. Image stacks were collected with a 200 nm step size between planes with 10 msec per plane exposure time and 14.8 sec time interval. After the acquisition, images were deskewed and deconvolved using LLSpy. After deskew processing, the voxel pitch was $0.104\times0.104\times0.103\mu$m.

Particle image velocimetry (PIV) analysis

PIV analysis was performed using PIVlab [45] for the time-lapse images obtained by LLSM. The velocity vector fields were calculated using a multi-grid interrogation (64×64, 32×32, and 16×16 pixel sizes of interrogation windows with 50% overlap each). PIV was performed in the masked area, and the masked area was determined by thresholding the time-integrated image. Using the velocity vector field (v_x, v_y), we first calculated azimuthal (v_φ) and radial (v_ρ) velocities as $v_\varphi = \hat{x}v_y - \hat{y}v_x$ and $v_r = \hat{x}v_x + \hat{y}v_y$, where $\hat{x} = x/r$ and $\hat{y} = y/r$ with (x, y) being the position from the center of cell and $r = \sqrt{x^2 + y^2}$. Here, the cell center was taken as the xy-coordinate of the highest position of the unimodal-shaped cell. From the DIC image, the nucleus always rotates around the center of the nucleus, with the highest position of the cell just above the nucleus center. Then, the angular velocity ω was obtained as $\omega = v_\varphi/r$. The temporal averages of v_φ and ω are shown in Fig. S4 for all samples analyzed (control cells (DMSO)(Figs. S4A-C) and cells treated with SMIFH2 (Figs. S4D-F)). The angular averages of v_φ (Fig. S4G), v_r (Fig. S4I) and ω (Fig. 6C) were obtained from their temporal averages at each spatial point. These averages were plotted against the radius scaled by the inner radius of the actomyosin ring in Fig. S4H, Fig. S4J and Fig. 6D. We here manually identified the inner edge of the actomyosin ring and calculated the inner radius for each cell.

Theoretical model

We here describe a brief derivation of our 3D model [32]. We assume a low Reynolds number limit, a steady state, and incompressibility. In the theory of active chiral fluid, the momentum conservation is represented as:

$$0 = \partial_\beta(\sigma^s_{\alpha\beta} + \sigma^e_{\alpha\beta} + \sigma^a_{\alpha\beta}), \tag{2}$$

where $\sigma^s_{\alpha\beta}$ and $\sigma^a_{\alpha\beta}$ are the symmetric and asymmetric parts of the deviatoric stress, respectively. $\sigma^e_{\alpha\beta}$ is Ericksen stress (hydrostatic stress). The indices α, β, and γ denote the three Cartesian coordinates x, y, and z. The constitutive equations of the deviatoric stress are given:

$$\sigma^s_{\alpha\beta} = 2\eta u_{\alpha\beta} + \zeta^a p_\alpha p_\beta, \tag{3}$$

$$\sigma^a_{\alpha\beta} = 2\eta'(\Omega_{\alpha\beta} - \omega_{\alpha\beta}), \tag{4}$$

where $u_{\alpha\beta} = (\partial_\alpha v_\beta + \partial_\beta v_\alpha)/2$ and $\omega_{\alpha\beta} = (\partial_\alpha v_\beta - \partial_\beta v_\alpha)/2$ is the strain rate and the vorticity. $\Omega_{\alpha\beta}$ is the spin rotation rate describing the intrinsic rotation rate of local volume elements. η and η' are viscosity coefficients, and ζ^a is a coefficient of the achiral active stress. We here only consider anisotropic contributions of active terms allowed in a chiral nematic active fluid for simplicity. Also, in this study, since we assume that the orientational field $\mathbf{p}$ is fixed to be a concentric pattern, we omit the terms that derive from the molecular field. We thus define $\sigma^e_{\alpha\beta} = -P\delta_{\alpha\beta}$, where P is the pressure serving as a Lagrange multiplier to satisfy the incompressibility.

The angular momentum conservation is given by the following equation:

$$\partial_\gamma M_{\alpha\beta\gamma} = 2\sigma^a_{\alpha\beta}, \tag{5}$$

where $M_{\alpha\beta\gamma}$ is the angular momentum flux. The constitutive equation is written as:

$$M_{\alpha\beta\gamma} = \kappa\partial_\gamma\Omega_{\alpha\beta} + \zeta^c\epsilon_{\alpha\beta\delta}p_\delta p_\gamma, \tag{6}$$

where κ is a dissipative coefficient and ζ^c is a coefficient of the active chiral stress which reflects the symmetry of the torque dipole represented in Fig. 7, which is called nematic chiral rod motor [32]. $\epsilon_{\alpha\beta\gamma}$ is the Levi-Civita symbol.

We derive the following equation of motion from Eqs. 2-6,

$$0 = -\partial_\alpha P + 2\eta\partial_\beta u_{\alpha\beta} + \partial_\beta\zeta^a p_\alpha p_\beta + \frac{1}{2}\partial_\beta\partial_\gamma\zeta^c\epsilon_{\alpha\beta\delta}p_\delta p_\gamma + \frac{\kappa}{4\eta'}\partial_\gamma^2\left(\partial_\beta P\delta_{\alpha\beta} - 2\eta\partial_\beta u_{\alpha\beta} - 2\partial_\beta\zeta^a p_\alpha p_\beta + 2\eta'\partial_\beta\omega_{\alpha\beta}\right). \tag{7}$$

In the final term of Eq. 7, the length scale $\ell = \sqrt{\kappa/\eta'}$ is a characteristic molecular scale. Since we consider the hydrodynamics at the cell scale, we take the limit of $\ell \to 0$ and omit the final term. Finally, applying the incompressibility condition $\partial_\gamma v_\gamma = 0$, we obtain the final form:

$$0 = -\partial_\alpha P + \eta\partial_\gamma^2 v_\alpha + \partial_\beta\zeta^a p_\alpha p_\beta + \frac{1}{2}\partial_\beta\partial_\gamma\zeta^c\epsilon_{\alpha\beta\delta}p_\delta p_\gamma, \tag{8}$$

which is equivalent to Eq. 1.

In the numerical simulations, for simplicity, we suppose that the cell is axisymmetric as shown in Figs. 7 and S5. Based on the experimental observations, we consider that the actomyosin bundles align along the circumferential direction: the concentric pattern of the actomyosin ring. We here represent the orientational order $\mathbf{p}$ of the actomyosin in the cylindrical coordinate (ρ, φ, z). Since $\mathbf{p}$ is aligned in the circumferential direction, $\mathbf{p}(\rho, z)$ is given in the cylindrical coordinate by

$$\mathbf{p}(\rho, z) = S(\rho, z)\,(0, 1, 0)^t\,, \tag{9}$$

where $S(\rho, z)$ is the effective strength of the orientation of the actomyosin and takes a finite value in the domain where the actomyosin ring is present. Since we did not see any specific orientational order in the direction of the cell height at least at our imaging resolution, we considered the orientation of the actomyosin bundle to be parallel to the substrate, and the z component of $\mathbf{p}(\rho, z)$ is zero. In the cylindrical coordinate, Eq. 1 of motion for the fluid velocity $\mathbf{v} = (v_\rho, v_\varphi, v_z)^t$ and the pressure P read

$$\eta\left(\partial_\rho^2 v_\varphi + \partial_z^2 v_\varphi + \frac{1}{\rho}\partial_\rho v_\varphi - \frac{1}{\rho^2}v_\varphi\right) = \frac{\zeta^c}{\rho}S\partial_z S, \tag{10}$$

$$\eta\left(\partial_\rho^2 v_\rho + \partial_z^2 v_\rho + \frac{1}{\rho}\partial_\rho v_\rho - \frac{1}{\rho^2}v_\rho\right) = \partial_\rho P + \zeta^a\frac{S^2}{\rho}, \tag{11}$$

$$\eta\left(\partial_\rho^2 v_z + \partial_z^2 v_z + \frac{1}{\rho}\partial_\rho v_z\right) = \partial_z P, \tag{12}$$

$$\frac{v_\rho}{\rho} + \partial_\rho v_\rho + \partial_z v_z = 0, \tag{13}$$

In order to numerically solve the set of equations, we assumed a cell shape where the dorsal boundary is given by

$$z = \begin{cases} Z_0 - r_0 + \sqrt{r_0^2 - \rho^2}, & (0 \le \rho \le r_0\sin\alpha) \\ -(\tan\alpha)(\rho - R_0), & (r_0\sin\alpha \le \rho \le R_0) \end{cases} \tag{14}$$

and the ventral boundary is specified with $z = 0$, as shown in Fig. S5. Here, $r_0 = (R_0\sin\alpha - Z_0\cos\alpha)/(1 - \cos\alpha)$ and Z_0, R_0 and α are the parameters that identify the cell shape. Also, since the actomyosin ring is located along the dorsal surface, in order to represent the localization numerically, we practically assume that $S(\rho, z)$ is given by

$$S(\rho, z) = (0.5\tanh\left(\lambda_1(\rho\sin\alpha + z\cos\alpha - \xi_1)\right) + 0.5) \times (0.5\tanh\left(\lambda_2(\rho\cos\alpha - z\sin\alpha - \xi_2)\right) + 0.5)\,, \tag{15}$$

where λ_i and ξ_i $(i = 1, 2)$ are parameters. An example of $S(\rho, z)$ is shown in Fig. 7B. We numerically solved the equations of motion by assuming the no-slip boundary condition for the ventral boundary, the free slip boundary condition for the dorsal surfaces, and the vanishing flow velocity for v_ρ and v_φ and the continuity for v_z at the cell center $\rho = 0$. We do not include any organelles such as a nucleus in the model for simplicity. The equations were solved numerically with a finite element method using software FreeFEM++ [46]. We used the following parameter values: $\eta = 1$, $\zeta^c = 0.4$, $\zeta^a = 1.0$, $Z_0 = 5$, $R_0 = 25$, $\alpha = 15°$, $\lambda_1 = 5$, $\lambda_2 = 0.5$, $\xi_1 = R_0\sin\alpha - 0.5$, $\xi_2 = 11.5$.

Quantification of dorsal and ventral actomyosin

Fluorescent signals of anti-myosin IIA and phalloidin were obtained by LSM880 (Zeiss) with Airyscan and processed by ImageJ Fiji. The obtained images were resliced and ten x-z slices containing the cell center were processed with mean intensity projection. The dorsal and ventral surfaces were manually traced with ten-pixels-width and the average signal intensities in the traced regions were quantified. The cell edge regions of overlapping dorsal and ventral traces were annotated as "peripheral region" and excluded from the quantification.

ACKNOWLEDGMENTS

This work was supported by Kakenhi grant 19K16096 (TY) 23K14186 (TI), 22H05170, 23H02455 (TS), and JST CREST Grant JPMJCR1852 (TS) and the core funding at RIKEN Center for Biosystems Dynamics Research. TY and TI were suported by Grant-in-Aid for JSPS Fellows 18J01239 (TY) and 22KJ3145 (TI). We thank H. Saito, T. Kato, and H. Hamada for the advice and support during experiments, M. Hayakawa, G.

Ogita, B. Bhattacherjee, R. Nishizawa, K. Kawaguchi, K. Adachi, Y. Fukai, R. Cerbus, T. Kato, S. Fürthauer, Y. H. Tee, and A. D. Bershadsky for fruitful discussions, and W. Kimura for sharing reagents.

[1] H. Hamada and P. P. L. Tam, F1000prime reports **6**, 110 (2014).
[2] M. Blum and T. Ott, Current Biology **28**, R301 (2018).
[3] S. R. Naganathan, S. Fürthauer, M. Nishikawa, F. Jülicher, and S. W. Grill, eLife **3**, e04165 (2014).
[4] L. G. Pimpale, T. C. Middelkoop, A. Mietke, and S. W. Grill, eLife **9**, e54930 (2020).
[5] K. Sugioka and B. Bowerman, Developmental Cell **46**, 257 (2018).
[6] Y. Shibazaki, M. Shimizu, and R. Kuroda, Current Biology **14**, 1462 (2004).
[7] A. Davison, G. S. McDowell, J. M. Holden, H. F. Johnson, G. D. Koutsovoulos, M. M. Liu, P. Hulpiau, F. V. Roy, C. M. Wade, R. Banerjee, F. Yang, S. Chiba, J. W. Davey, D. J. Jackson, M. Levin, and M. L. Blaxter, Current Biology **26**, 654 (2016).
[8] M. Abe and R. Kuroda, Development **146**, dev175976 (2019).
[9] S. Hozumi, R. Maeda, K. Taniguchi, M. Kanai, S. Shirakabe, T. Sasamura, P. Spéder, S. Noselli, T. Aigaki, R. Murakami, and K. Matsuno, Nature **440**, 798 (2006).
[10] K. Taniguchi, R. Maeda, T. Ando, T. Okumura, N. Nakazawa, R. Hatori, M. Nakamura, S. Hozumi, H. Fujiwara, and K. Matsuno, Science **333**, 339 (2011), 10.1126/science.1200940.
[11] R. Hatori, T. Ando, T. Sasamura, N. Nakazawa, M. Nakamura, K. Taniguchi, S. Hozumi, J. Kikuta, M. Ishii, and K. Matsuno, Mechanisms of development **133**, 146 (2014-08).
[12] K. Sato, T. Hiraiwa, E. Maekawa, A. Isomura, T. Shibata, and E. Kuranaga, Nature Communications **6**, 10074 (2015).
[13] P. Ray, A. S. Chin, K. E. Worley, J. Fan, G. Kaur, M. Wu, and L. Q. Wan, Proceedings of the National Academy of Sciences **115**, E11568 (2018).
[14] T. Ishibashi, R. Hatori, R. Maeda, M. Nakamura, T. Taguchi, Y. Matsuyama, and K. Matsuno, Genes to Cells **24**, 214 (2019).
[15] A. Tamada, S. Kawase, S. Kawase, F. Murakami, F. Murakami, H. Kamiguchi, and H. Kamiguchi, The Journal of Cell Biology **188**, 429 (2010).
[16] H. Yamanaka and S. Kondo, Genes Cells **20**, 29 (2015-01).
[17] Y. H. Tee, T. Shemesh, V. Thiagarajan, R. F. Hariadi, K. L. Anderson, C. Page, N. Volkmann, D. Hanein, S. Sivaramakrishnan, M. M. Kozlov, and A. D. Bershadsky, Nature Cell Biology **17**, 445 (2015-04).
[18] Y. H. Tee, W. J. Goh, X. Yong, H. T. Ong, J. Hu, I. Y. Y. Tay, S. Shi, S. Jalal, S. F. H. Barnett, P. Kanchanawong, W. Huang, J. Yan, Y. A. B. Lim, V. Thiagarajan, A. Mogilner, and A. D. Bershadsky, Nature Communications **14**, 776 (2023).
[19] A. S. Chin, K. E. Worley, P. Ray, G. Kaur, J. Fan, and L. Q. Wan, Proceedings of the National Academy of Sciences **115**, 12188 (2018).
[20] T.-H. Chen, J. J. Hsu, X. Zhao, C. Guo, M. N. Wong, Y. Huang, Z. Li, A. Garfinkel, C.-M. Ho, Y. Tintut, and L. L. Demer, Circulation Research **110**, 551 (2012).
[21] K. Sato, T. Hiraiwa, and T. Shibata, Physical Review Letters **115**, 188102 (2015).
[22] T. Yamamoto, T. Hiraiwa, and T. Shibata, Physical Review Research **2**, 043326 (2020).
[23] N. A. Brown and L. Wolpert, Development **109**, 1 (1990).
[24] J. Xu, A. V. Keymeulen, N. M. Wakida, P. Carlton, M. W. Berns, and H. R. Bourne, Proceedings of the National Academy of Sciences **104**, 9296 (2007).
[25] T. Nishizaka, T. Yagi, Y. Tanaka, and S. Ishiwata, Nature **361**, 269 (1993).
[26] I. Sase, H. Miyata, S. Ishiwata, and K. Kinosita, Proceedings of the National Academy of Sciences **94**, 5646 (1997).
[27] M. Ozawa, S. Hiver, T. Yamamoto, T. Shibata, S. Upadhyayula, Y. Mimori-Kiyosue, and M. Takeichi, Journal of Cell Biology **219**, e202006196 (2020).
[28] S. Tojkander, G. Gateva, and P. Lappalainen, Journal of Cell Science **125**, 1855 (2012).
[29] A. L. Miller and W. M. Bement, Nature Cell Biology **11**, 71 (2009).
[30] B. Nolen, N. Tomasevic, A. Russell, D. Pierce, Z. Jia, C. McCormick, J. Hartman, R. Sakowicz, and T. Pollard, Nature **460**, 1031 (2009).
[31] S. A. Rizvi, E. M. Neidt, J. Cui, Z. Feiger, C. T. Skau, M. L. Gardel, S. A. Kozmin, and D. R. Kovar, Chemistry & Biology **16**, 1158 (2009).
[32] S. Fürthauer, M. Strempel, S. W. Grill, and F. Jülicher, The European Physical Journal E **35**, 89 (2012-09).
[33] S. Fürthauer, M. Strempel, S. W. Grill, and F. Jülicher, Physical Review Letters **110**, 048103 (2013).
[34] E. Tjhung, M. E. Cates, and D. Marenduzzo, Proceedings of the National Academy of Sciences **114**, 4631 (2017), 1706.07723.
[35] A. Kumar, A. Maitra, M. Sumit, S. Ramaswamy, and G. V. Shivashankar, Scientific Reports **4**, 3781 (2014).
[36] N. D. Bade, R. D. Kamien, R. K. Assoian, and K. J. Stebe, Science Advances **3**, e1700150 (2017).
[37] R. Kuroda, K. Fujikura, M. Abe, Y. Hosoiri, S. Asakawa, M. Shimizu, S. Umeda, F. Ichikawa, and H. Takahashi, Scientific Reports **6**, 34809 (2016).
[38] T. C. Middelkoop, J. Garcia-Baucells, P. Quintero-Cadena, L. G. Pimpale, S. Yazdi, P. W. Sternberg, P. Gross, and S. W. Grill, Proceedings of the National Academy of Sciences **118**, e2021814118 (2021).
[39] M. Tarama and T. Shibata, Physical Review Research **4**, 043071 (2022), 2109.00841.
[40] Q. Ni, K. Wagh, A. Pathni, H. Ni, V. Vashisht, A. Upadhyaya, and G. A. Papoian, eLife **11**, e82658 (2022).
[41] S. Nakamura, I. Grigoriev, T. Nogi, T. Hamaji, L. Cassimeris, and Y. Mimori-Kiyosue, PLoS ONE **7**, e51442 (2012).
[42] C. Zhang, J. S. Kang, S. M. Asano, R. Gao, and E. S. Boyden, Current Protocols in Neuroscience **92**, e96 (2020).
[43] C. E. Park, Y. Cho, I. Cho, H. Jung, B. Kim, J. H. Shin, S. Choi, S.-K. Kwon, Y. K. Hahn, and J.-B. Chang, ACS

Nano **14**, 14999 (2020).

[44] B.-C. Chen, W. R. Legant, K. Wang, L. Shao, D. E. Milkie, M. W. Davidson, C. Janetopoulos, X. S. Wu, J. A. Hammer, Z. Liu, B. P. English, Y. Mimori-Kiyosue, D. P. Romero, A. T. Ritter, J. Lippincott-Schwartz, L. Fritz-Laylin, R. D. Mullins, D. M. Mitchell, J. N. Bembenek, A.-C. Reymann, R. Böhme, S. W. Grill, J. T. Wang, G. Seydoux, U. S. Tulu, D. P. Kiehart, and E. Betzig, Science **346**, 1257998 (2014).

[45] W. Thielicke and R. Sonntag, Journal of Open Research Software **9**, 12 (2021).

[46] F. Hecht, Journal of Numerical Mathematics **20**, 251 (2012).